Electromagnetic Science
vol. 2, no. 1, 0050212, March 2024
https://doi.org/10.23919/emsci.2023.0021

Research Article

Frequency-Diversified Space-Efficient Radiating Surface Using Convolved Electric and Magnetic Currents for Highly Dense Multiband Antenna-Frontend Integration

Amirhossein Askarian, Pascal Burasa, and Ke Wu

Department of Electrical Engineering, Poly-Grames Research Center, Polytechnique Montreal, QC H3T1J4, Canada

Corresponding author: Amirhossein Askarian, Email: a.askarian@polymtl.ca.
Received June 9, 2023; Accepted July 22, 2023; Published Online February 2, 2024.

Abstract — We propose and investigate a methodology based on convolved electric and magnetic currents for the generation of multi-band responses over a space-shared radiating surface. First, a single wideband antenna operation principle based on interleaved dipole and slot modes is studied and analyzed using full-wave simulations followed by a qualitative time domain analysis. Subsequently, a 2 × 2 dual-band radiating unit is conceived and developed by closely arranging single wideband antennas. In this case, multimode resonances are generated in a lower frequency band by a proper convolving and coupling of the magnetic and electric currents realized in the gaps between the antennas and on the surface of the antennas, respectively. This methodology can be deployed repeatedly to build up a self-scalable topology by reusing the electromagnetically (EM) connected radiating surfaces and gaps between the radiating units. Due to the efficient reuse of the electromagnetic region for the development of multiband radiation, a high aperture-reuse efficiency is achieved. Finally, as a proof of concept, a 2 × 4 dual-band array operating in Ku- and Ka-bands is developed and fabricated by a linear arrangement of the two developed radiating units. Our measurement results show that the proposed antenna array provides impedance and gain bandwidths of 30% and 25.4% in the Ku-band and 10.65% and 8.52% in the Ka-band, respectively.

Keywords — Aperture-shared array, Aperture-reused efficiency, Antenna-frontend integration, Dual-band antenna, Magneto-electric dipole antenna, Multi-mode resonance, Multi-band array, Multi-functional antenna, Wideband antenna array.

Citation — Amirhossein Askarian, Pascal Burasa, and Ke Wu, "Frequency-diversified space-efficient radiating surface using convolved electric and magnetic currents for highly dense multiband antenna-frontend integration," *Electromagnetic Science*, vol. 2, no. 1, article no. 0050212, 2024. doi: 10.23919/emsci.2023.0021.

I. Introduction

The progress of wireless technology development over the past decades has fundamentally been fueled by an ever-increasing demand for efficient communication links related to our constantly changing information era. This progress is set to revolutionize the next generation technology not only for data communication but also for parametric sensing and wireless powering [1], [2]. This has undoubtedly sparked the curiosity in the R&D community towards the development of multifunction frontends [3], [4]. Among such newly emerging 5G and 6G wireless joint communication and sensing technologies as analogue radio-over-fiber (ARoF) systems, the development of multifunction systems with the virtue of gigabit throughput and multispectral sensing based on frequency-diversity is of crucial advantage. A successful implementation of those frontends requires cutting-edge techniques to address different technological issues in both microwave and millimeter-wave (mmW) bands. To realize multifunction wireless systems, space-efficient multi-band antenna solutions featuring high-gain, low-complex, and easy to in situ integration with active circuits are incontestably essential.

Multi-band antenna arrays simultaneously operating in both the microwave and mmW bands have been extensively investigated and reported in the literature [5]–[28]. However, developing a space-efficient multiband antenna array

for such highly integrated multifunction frontends is fundamentally challenging and still requires more exploration. Aperture-shared techniques, which make use of a common radiating surface for the development of multiband antenna array, offer a promising methodology for addressing the requirements of such space- and power-efficient antenna-frontend integration. Thus far, a majority of published studies on dual-band antennas and particularly tri-band aperture-shared antennas [26]–[28] have been generally based on stacking multilayers or interleaving topologies of different types of antenna elements in a single layer and using complex feeding networks, which not only incur unnecessary fabrication costs but also make the cohabitation of active circuits and antennas practically impossible.

Numerous practical techniques have been suggested in open literature for realizing planar dual band aperture-shared antenna arrays, such as patch and DRA antennas [8], segmented patch antennas [9], SIW cavity-based slot antenna arrays [10], [12], grid arrays [11], Fabry-Perot cavities [14], [16]–[20], [28], Fabry-Perot cavity and Fresnel zone plates [15], metasurfaces [21]–[23], multimode resonance slots [24], and perforated patch antenna arrays [7], [27]. However, they still exhibit relatively low impedances and gain bandwidths despite the use of low permittivity materials. Hence, a methodology based on using high-κ materials for the development of multiband antenna arrays that can also present both reasonable gain and impedance bandwidth remains an unsolved challenge despite its practical and technological significance.

The magneto-electric dipole (ME-dipole) antennas, which have also been known as complementary-source antennas, are popular for offering broad impedances and gain bandwidths, low cross-polarization, and high radiation and aperture efficiency [29]–[36]. A half-wavelength dipole and a quarter-wavelength patch antenna were utilized in a conventional manner to serve as electric and magnetic currents, respectively [36]. Thus far, there is still a crucial need to adopt the ME-dipole concept for the development of a planar multiband radiating surface-featuring broad bandwidths, space efficiency, and ease of cohabitation with active circuits. On the other hand, a seamless integration of antenna with active circuits in a highly integrated frontend module, is of practical and technological importance, as this scheme is set to eliminate the need for bonding wires and their associated parasitic effects, excessive losses, and costs. In this case, the antenna array is implemented in an identical fabrication process as the active elements. In this connection, the antenna array should be implemented in a high-κ material, such Si and SiGe, which severely degrades the antenna array performances due to the adverse effects of surface waves and associated mutual couplings [37]–[39].

In addition, it is worth mentioning that as the permittivity (or permeability) in a conventional antenna array design is increased, the physical size of the antenna is decreased while the inter-element spacing is maintained constant (to avoid increasing mutual coupling caused by space waves), resulting in the excitation of higher-order surface wave modes. Indeed, there is a crucial need for the development of multi-band antenna arrays with not only the above-mentioned features, but also the ability to suppress surface waves on the aperture without adding any potential complexity to the antenna structure.

In this work, a topological and scalable multiband radiating surface operating based on convolved electric and magnetic surface currents, resulting in broad impedance and gain bandwidth, is proposed, investigated, and demonstrated. Due to an efficient reuse of the antenna aperture in all frequency bands of interest, the proposed radiating surface features high aperture-reused efficiency. This aperture-reused efficient radiating surface is an appropriate candidate for seamless antenna-frontend integration (unified circuit-antenna) design scenarios [39]. Due to the boundary condition realized by a tight arrangement of metallic radiating elements, surface waves are weakly excited (or not excited) on the antenna aperture. With a planarized structure of the proposed radiating surface, a technique based on the use of both low permittivity and high permittivity (high-κ) substrates is adopted in the proposed architecture to take advantages of using both low and high permittivity materials for radiation and integration purposes, respectively. In fact, this heterogeneous architecture is compatible with cost-effective yet mature fabrication processes such as the CMOS process. Then, as a proof of concept, we devise a dual-band radiating unit as the fundamental building block of the proposed topological radiating surface. The simulation and measurement results suggest the practical feasibility and confirm the efficient reuse of space for the development of a frequency-diversity radiating surface, while maintaining reliable radiation performances and coherent beam directions.

This paper is organized as follows. In Section II, we introduce and study the proposed topological multiband radiating surface concept along with its potential challenges. In Section III, the antenna element operating based on convolved electric and magnetic currents is thoroughly analyzed. A parametric analysis is then conducted for a further investigation about the feasibility of the cohabitation of active circuits antenna. In Section IV, the dual-band radiating unit is developed and studied in both lower and upper frequency bands. In Section V, the structure of the developed dual-band antenna array in both the Ku-band and Ka-band, full-wave simulation and measurement results are presented. A comparison is also provided to highlight the performance of the proposed structure with the published results.

II. General Topology and Concept

The general concept and topology of the proposed multiband radiating surface is shown in Figure 1(a). The topology makes use of both the electric and magnetic surface currents, which respectively correspond to the dipole and slot modes, in three different polarizations convolved together to generate three radiating modes (f_H, f_M, and f_L). Al-

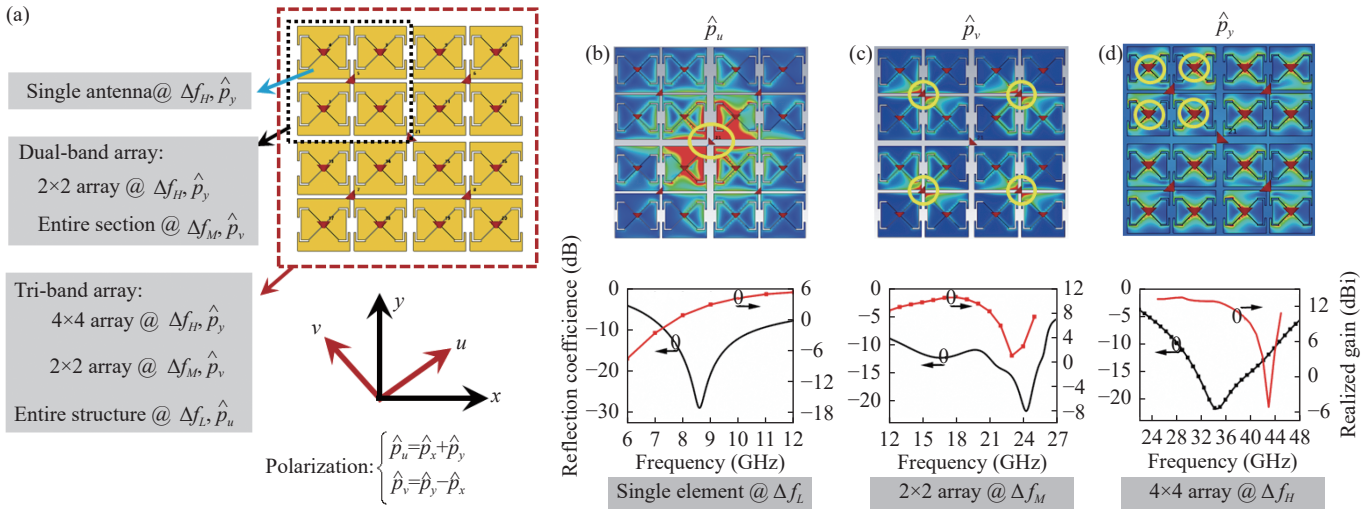

Figure 1 (a) General demonstration of the proposed topology and concept for generating three radiating modes; (b)–(d) Full-wave simulation results including surface current distributions, reflection coefficients, and realized gains in different frequency bands.

though the presented topology generates three radiating modes, it could theoretically be extended to the scenario of a multimode radiating surface operating at several radiating modes. As suggested by the surface currents distributions in Figures 1(b)–(d), the individual $\hat{y}$-polarized antenna (radiating element with $\hat{p}_y$ polarization) radiates at the highest frequency band (Δf_H), the 2 × 2 arrangement of four radiating elements (an array of 2 × 2) with polarization toward v-axis ($\hat{p}_v$) works at the middle frequency band (Δf_M) , and the entire radiating surface that is polarized along the u-axis ($\hat{p}_u$) operates at the lowest frequency bands (Δf_L).

By implementing proper edge gaps between each antenna as well as groups of antennas (c.f. Figure 1), the radiating surface can operate locally in the upper frequency band. As the frequency decreases, the antennas or groups of antennas are virtually merged and recast by mutual coupling, leading to a larger radiating surface that operates at the lower frequency bands. In the proposed topology shown in Figure 1, lump ports with proper orientations have been deployed to excite the three modes on the surface. Generally, each radiating section can be driven by integrated front-end active components.

The proposed topological radiating surface operates based on a local excitation of slot and dipole modes. Therefore, it does not require the support of a ground plane for radiation. As a result, the proposed antenna is referred to as a "radiating surface" throughout the paper. Since a ground plane is an indispensable part of an integrated circuit-antenna design scenario, we consider its effects in our investigation. Although the ground plane typically enhances the directivity and gain of an antenna, it can potentially limit the impedance and gain bandwidth of the radiating surface. According to the transverse equivalent network (TEN) model of the radiating surface, in a dual-band radiating surface with a frequency ratio of 2 in the lower frequency bands, the ground plane exhibits inductive effects on the input impedance of excitation sources, while it has a capacitive effect in the upper-frequency bands. In addition, the proposed topological antenna array can theoretically be extended to operate in several frequency bands (a multi-band radiating surface). However, the ground plane might restrict the number of frequency bands, as well as frequency ratio between multiple bands.

In contrast to the metasurface-based antenna radiation based on fringing fields [40], in the proposed topological radiating surface, the minimum distance between the ground plane and the radiating surface should be selected larger than $\lambda_{gL}/10$ [λ_{gL} is the maximum guided wavelength at the lowest frequency band (Δf_L)] to avoid sever gain loss due to virtual short circuit. In addition, it should be smaller than $\lambda_{gH}/2$ [λ_{gH} is the minimum guided wavelength at the upper frequency band (Δf_H)] to prevent the structure from the formation of a Fabry-Perot cavity between the radiating surface [acts as a partially reflecting surface (PRS)] and the ground plane. In the latter case and according to the planar leaky-wave theory [6], [38], the gain profile experiences a deep null just before and after the cavity resonance, while it shows a crest (highly directive radiation pattern) corresponding to the cavity resonance. As a result, the in-band gain profile has severe fluctuations as the frequency changes, which reduce the gain bandwidth. In the next sections, the principle of a dual-band radiating surface, as the fundamental building block of the proposed topological radiating surface, is investigated. Initially, the antenna working at the highest frequency band is analyzed. Then, it is shown that the arrangement of four antennas as a group of 2 × 2 can radiate in the lower frequency band based on convolving magnetic and electric surface currents.

III. Fundamentals of the Radiating Element

Figure 2 shows the antenna geometry along with the reflection coefficient, gain profile, and radiation patterns at several frequencies ranging from 25 to 50 GHz. The antenna contains two parasitic elements as well as two driven parts,

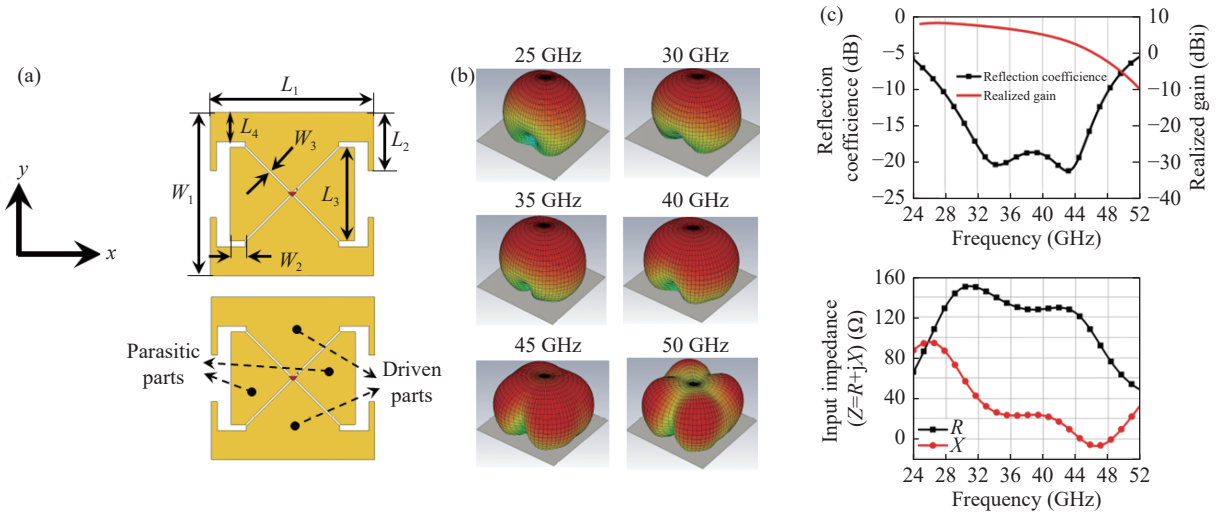

Figure 2 (a) Geometry of the proposed antenna based on the coupled electric and magnetic surface currents, $L_1 = W_1 = 4.2$ mm, $L_2 = 1.5$ mm, $W_2 = 0.26$ mm, $L_3 = 2.4$ mm, $W_3 = 0.05$ mm, $L_4 = 0.75$ mm; (b) Radiation patterns of the antenna in several frequency bands; (c) Reflection coefficient, gain profile, and input impedance of the antenna.

which are excited along the y-axis at the antenna center by a lumped port in the CST Microwave Studio. Moreover, the antenna is placed at the distance of 2.7 mm above the ground plane. As indicated in Figure 2(c), an impedance and gain bandwidth as wide as 52.6% is achieved by the coupling of the dipole and slot modes (magnetic and electric currents, respectively) to generate a multimode resonance (MMR) behavior, as depicted in the input impedance diagram.

Although the slot and dipole modes are generally coupled and convolved, individual contributions of each mode can be investigated, as shown in Figure 3. In $0 \le \varphi < \pi/2$, through a frequency-domain analysis, the antenna corresponding to $0 \le t < T/4$ with a time-domain analysis ($\varphi = \omega t$) radiates based on the two diagonally oriented slots or equivalently magnetic currents along with the u-axis and v-axis in which $\vec{M}_v = \vec{M}_y - \vec{M}_x$ and $\vec{M}_u = \vec{M}_x + \vec{M}_y$. For $\pi/2 \le \varphi < \pi$ corresponding to $T/4 \le t < T/2$ in a time-domain analysis, the contribution of the dipole mode outweighs that of the slot mode and antenna radiates as u and v-polarized electric surface currents in which $\vec{J}_v = \vec{J}_y - \vec{J}_x$, and $\vec{J}_u = \vec{J}_x + \vec{J}_y$. As a result, two sets of coupled and interleaved magnetic and electric currents $\{(\vec{J}_x, \vec{M}_y), (\vec{J}_y, \vec{M}_x)\}$ contribute to the antenna's operations.

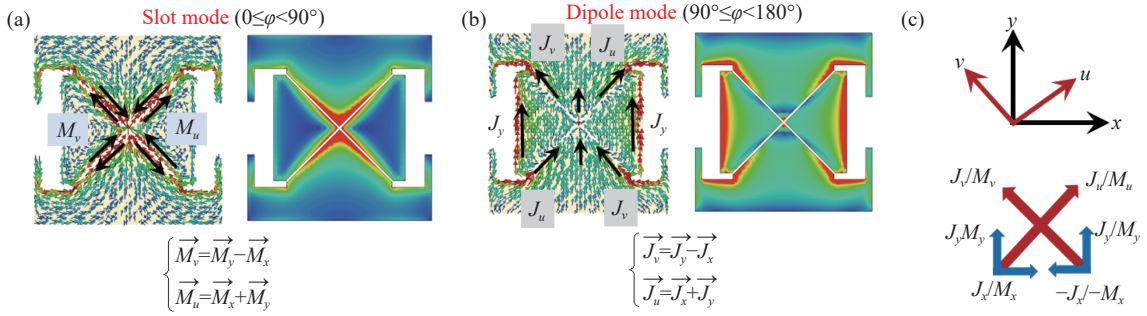

Figure 3 Surface currents on the proposed ME-dipole-alike antenna in (a) The slot mode and (b) Dipole mode and (c) The illustration of the convolved electric and magnetic surface currents.

In the proposed antenna with coupled slot and dipole modes, the effective electrical size of the dipole and slot modes is somewhat larger than the resonance length. Thus, the input impedance of the individual dipole mode is inductive, while it is capacitive for the slot mode. Therefore, from the perspective of the equivalent circuit model (ECM), this antenna can be represented as a parallel combination of a capacitance and an inductor that are connected to an AC source. As a result, the capacitor and inductor are periodically charged and discharged on different time slots. According to the ECM and electrical circuit theory, during $0 \le t < T/4$, the capacitor (i.e., slot mode) is charged. Then, in $T/4 \le t < T/2$, the capacitor is discharged. Concurrently, the current of the inductor (dipole mode) increases. Therefore, in the first time slot, the proposed antenna mainly operates based on the slot mode, while in the second time slot, the dipole mode is the dominant mode of the radiation. As such, the antenna operates based on exchanging energy

between the slot and dipole modes. In this scenario, since both the slot and dipole modes contribute to the operation of the antenna, this antenna radiates based on the ME-dipole concept and is called the ME-dipole-alike antenna throughout this paper.

With reference to Figure 2(c), the realized gain of the ME-dipole-alike antenna experiences a steep reduction at the end of the band, which can be explained by examining the surface current distributions along with 3D radiation patterns in different frequency bands, as shown in Figure 4. At 30 GHz, the antenna radiates based on the contributions of both u and v-directed magnetic and electric currents over the antenna surface. In this case, the antenna primarily radiates based on the contributions of the surface currents around the crossed-slots as well as two currents induced at the left and right ends of the parasitic parts along the y-axis. However, at frequencies above 40 GHz, a new set of surface currents (marked with red color) along the x-axis are emerged on the top and bottom of the driven parts, which are out-of-phase along both the x- and y-axes. Moreover, as the frequency increases, their contributions to the total surface currents are also increased. These surface currents are in-phase along the u- and v-axes. However, their total contribution to the radiation pattern at the broadside is out-of-phase, leading to the formation of a null at the broadside. Consequently, the gain profile in Figure 2(c) experiences a significant reduction for frequencies above 45 GHz.

The parametric analysis of some pivotal parts of the antenna provides more insights into the principle of the operation of the antenna. In this analysis, the variations of the input impedance with respect to the changing of some crucial parameters, which is of importance for direct integration of the antenna with active circuits, are investigated. Figure 5 depicts the profiles of the real and imaginary parts of the input impedance with respect to the variations of W_2 (W_2 in Figure 2(a)). In this case, the length of the electric current [c.f. Figure 3(b)] is changed, which, in turn, modifies the reactive effects (capacitive or inductive effects) of the impedance for the dipole mode. As a result, the coupling between the slot and dipole modes is switched between under coupled (with $W_2 = 1$ mm), coupled (with $W_2 = 1.4$ mm and 1.6 mm), and over coupled (with $W_2 = 1.8$ mm) resonance conditions in the proposed ME-dipole-alike antenna.

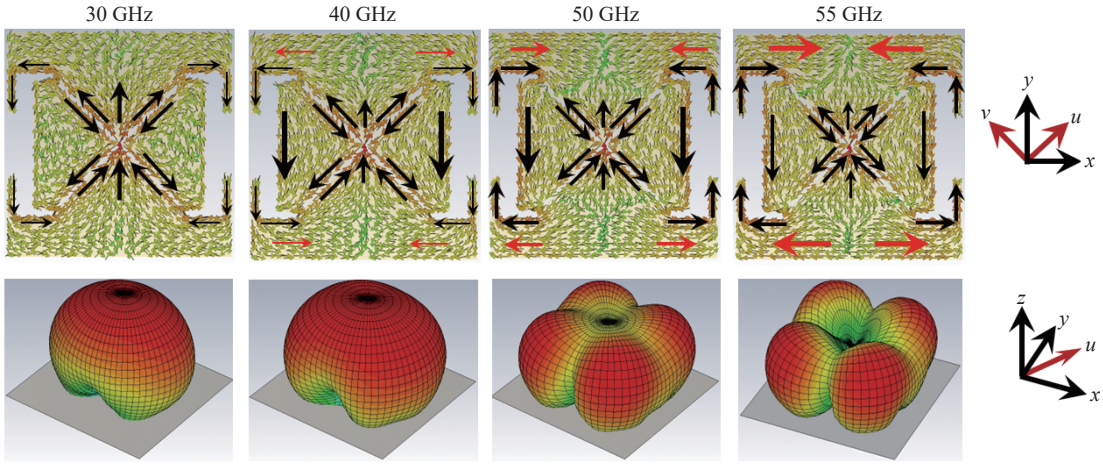

Figure 4 Distribution of the surface current along with radition patterns at four frequencies (30, 40, 50, and 55 GHz).

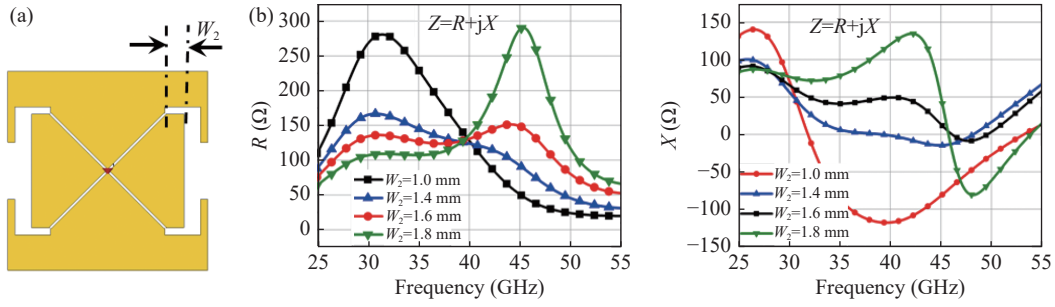

Figure 5 Parametric analysis of W_2 and its effects on the input impedance of the antenna.

In Figure 6, the feeding position is swept along the vertical direction by changing of ΔP. Consequently, the real part of the input impedance is swept over a wide frequency range while the imaginary part remains almost unchanged. This parameter would be crucial for integration as it provides an independent control on the real part of impedance.

Figure 7 provides a parametric analysis of several pa-

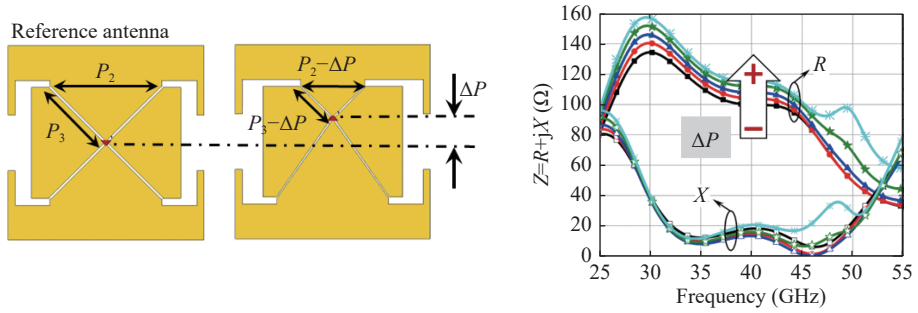

Figure 6 Parametric analysis of ΔP and its effects on the input impedance of the antenna.

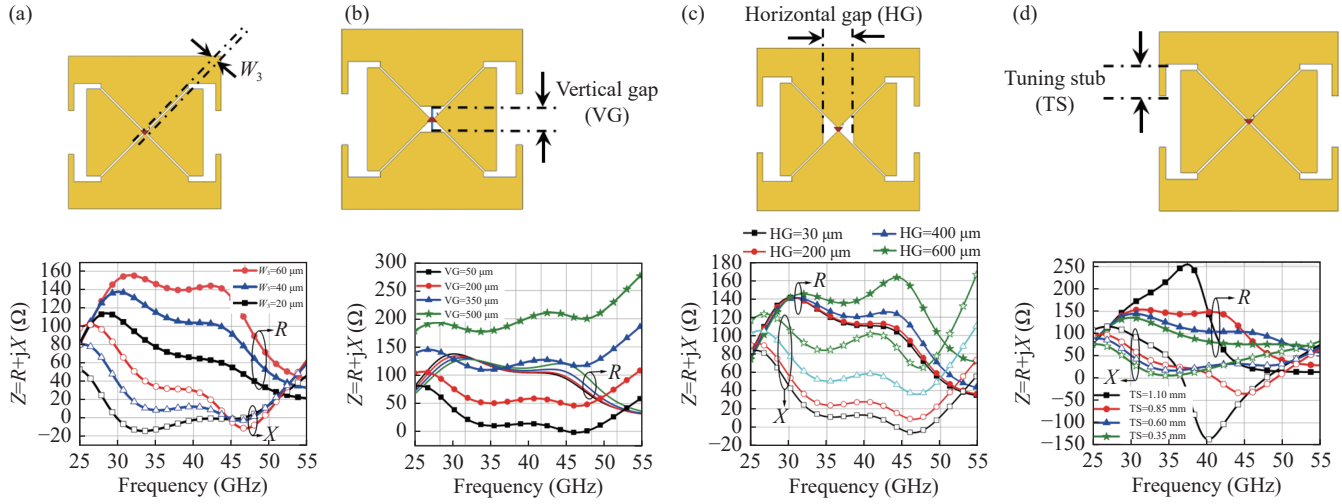

Figure 7 Variations of several critical parameters in the antenna and their effects on the input impedance of the antenna over a wide range of frequency.

rameters and their effects on the input impedance of the ME-dipole-alike antenna. As can be seen, changing both vertical and horizontal gaps in Figures 7(b) and (c) mainly affect the imaginary part of the impedance, while the real part is almost maintained unchanged over a wide frequency range. These two parameters are pivotal for directed conjugate matching between the antenna and active components without using a matching network.

IV. Dual-Band Radiating Unit

1. Lower frequency band

A dual-band radiating unit is realized by a 2 × 2 arrangement of the four ME-dipole antennas in proximity to make up a larger radiating surface in the lower frequency band, as shown in Figure 8. In this scenario, a diagonally oriented excitation (Port 5, along the v-axis) can excite both the electric surface current (along the x- and v-axes) on the antenna surface and magnetic surface currents in the slots ["gap" between the antennas along x- and y-axes, c.f. Figure 8(a)]. Similar to the ME-dipole-alike antenna, this structure also operates based on the convolving of two sets of magnetic and electric surface currents $\{(\vec{J}_x, \vec{M}_y), (\vec{J}_y, \vec{M}_x)\}$, as demonstrated in Figure 8(a).

By optimizing the dimensions as well as the gap between the antennas, a new set of slot and dipole modes is coupled, which results in a multi-mode resonance behavior, wide impedance and gain bandwidth, and symmetric radiation patterns over a wide range of frequency, as depicted in Figure 8(b). The maximum realized gain is approximately 6.5 dBi at 18 GHz, while it is reduced as the frequency decreases (due to small electrical distance between the radiating surface and the ground plane). Moreover, the gain is decreased at the upper end of the frequency band due to the formation of side lobes, as illustrated in Figure 8(b).

Parametric analysis of the inter-element gap [c.f. Figure 8(a)] on the antenna operations is investigated in Figure 9. A Smith chart diagram is used as it is more informative for illustrating the coupling between the slot and dipole modes. With reference to Figure 9(a), as the gap width is increased, the ring in the Smith chart, indicating the coupling between the slot and dipole modes, gradually becomes larger, indicating a looser coupling between the dipole and slot modes.

On the contrary, the coupling between the slot and dipole modes (or magnetic and electric currents) are tighter as the gap width is decreased. Considering the normalized input impedance of the antenna as $\overline{Z}_{in} = \overline{R} + j\overline{X}$ and with reference to its trajectory on the Smith chart, as the gap width is increased, both $\overline{R}$ and $\overline{X}$ are increased, as is highlighted in Figure 9(a) by the yellow arrow. Moreover, as the gap is increased in a specific range, the input impedance not only

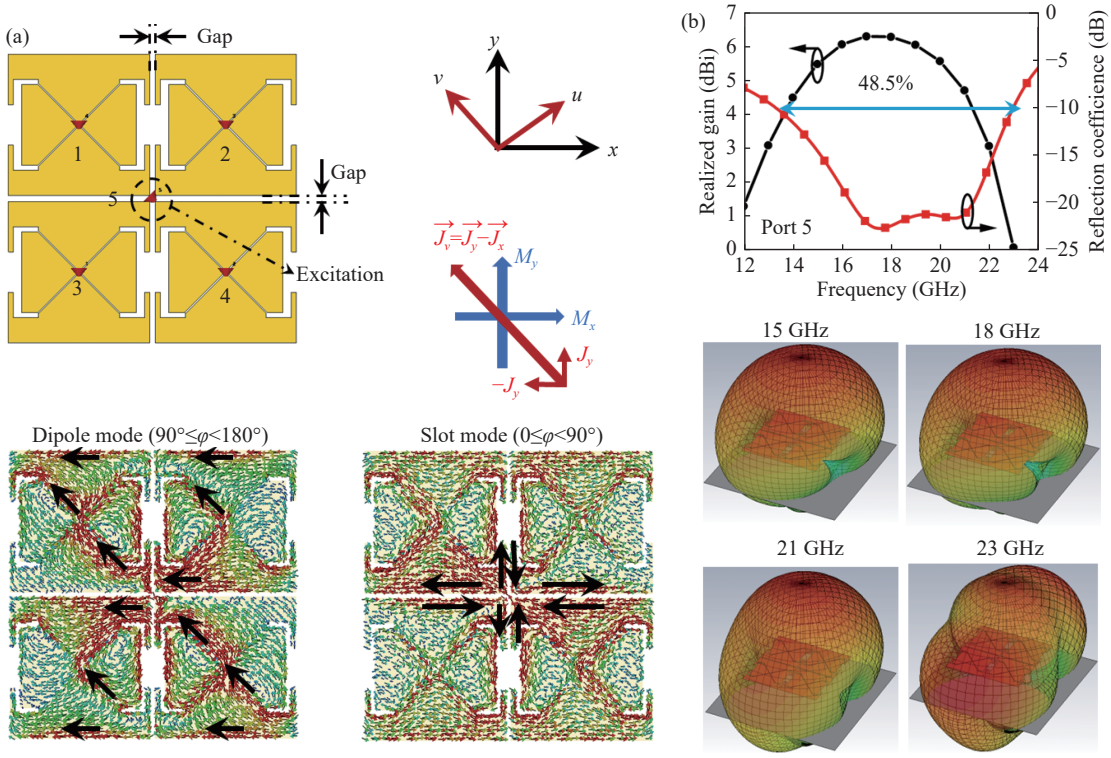

Figure 8 (a) Dual-band radiating unit realized by 2 × 2 arrangement of the four ME-dipole-alike antennas along with a distribution of the surface currents for both the dipole and slot modes in the lower frequency band; (b) The reflection coefficient, gain, and radiation patterns at four frequencies (15, 18, 21, and 23 GHz) in the lower frequency band.

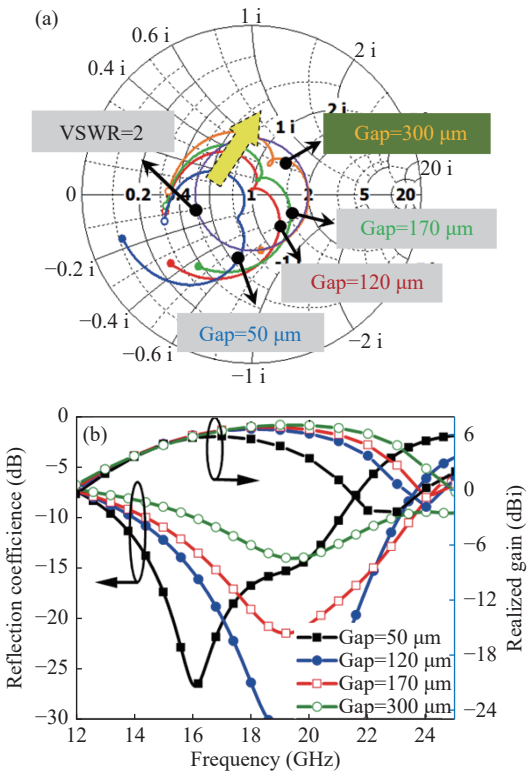

Figure 9 Effects of the different gap widths (50, 120, 170, and 300 μm) on the antenna performances, including (a) The input impedance and (b) Realized gain in the lower frequency band.

becomes more inductive, but the radiation resistance and consequently the antenna gain are also increased. It is verified by full-wave simulations in Figure 9(b) that the gain is increased with a larger value of the gap width.

In other words, in the over-coupled dipole-slot scenario ($f_{dipole} \approx f_{slot}$), which is realized with a smaller gap width, the antenna operates almost as a single resonator (dipole mode), as a result the peak gain and gain bandwidth are decreased. This analysis shows how properly coupled magnetic and electric currents can enhance the radiation properties of the antenna. It is worth mentioning that as the impedance matching and eventually impedance bandwidth ($VSWR \leq 2$) highly depend on the reference impedance (the source impedance at port 5 which is $R_s = 150\,\Omega$), the impedance bandwidth highly depends on the value of source impedance. Therefore, it can decrease or increase with respect to the variations of the gap width. This analysis clearly shows the effects of the gap between the antennas on formation and coupling of the dipole and slot resonance modes as well as its effects on the radiation performance in the lower frequency band.

2. Upper frequency band

In the upper frequency band, the ME-dipole antennas are excited individually by Ports 1–4 along the y-axis, as shown in Figure 10(a). Due to the multi-mode resonance behavior of the coupled electric (mostly along the y-axis) and magnetic currents (along the u- and v-axes), a wide impedance and gain bandwidth with stable radiation patterns is real-

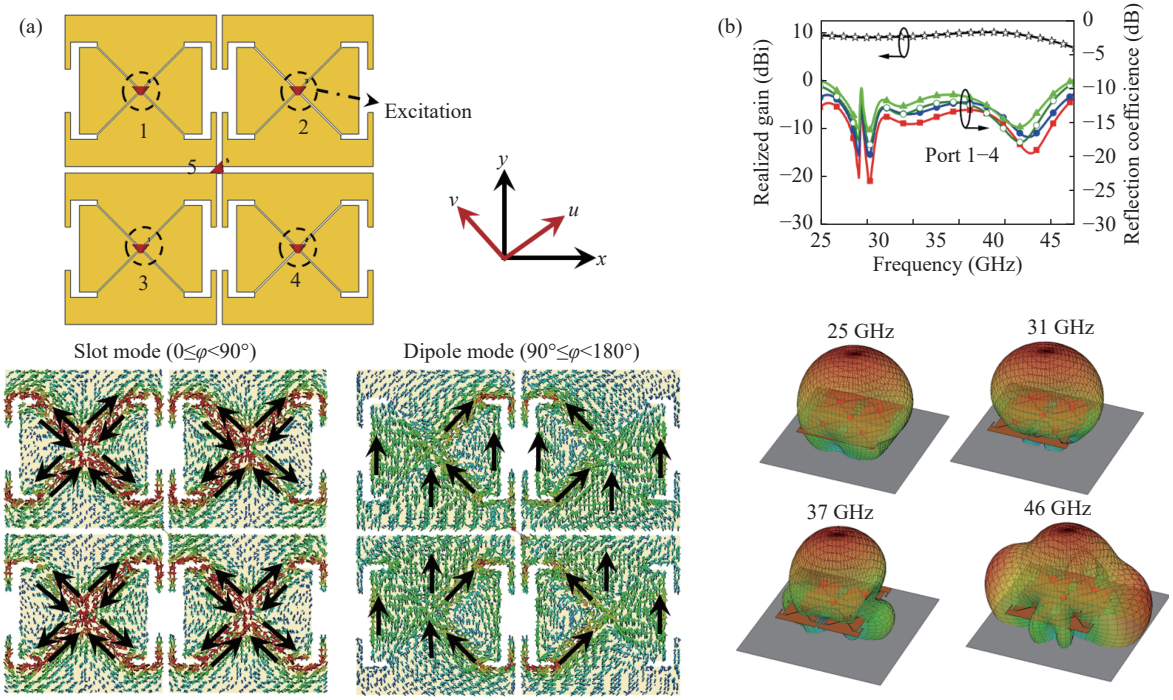

Figure 10 (a) Dual-band radiating unit realized by a 2 × 2 arrangement of four ME-dipole antennas along with a distribution of the surface currents for both dipole and slot modes in the upper frequency band, and (b) Reflection coefficient, gain, and radiation patterns in the lower frequency band.

ized, as depicted in Figures 10(a) and (b). With reference to Figure 10(b), the side lobes are formed at frequencies above 37 GHz, and these unwanted radiations cause a gain loss at the broadside at frequencies above 45 GHz.

Since in the lower frequency band, the radiations are based on the magnetic and electric currents along the direction of $(\hat{x},\hat{y})$ and $(\hat{x},\hat{v})$, respectively, while in the upper frequency band, they are along the $\hat{y}$ and $(\hat{u},\hat{v})$ axes, the dual band radiating surface basically operates based on convolving the magnetic and electric currents oriented in different directions, as summarized in Table 1.

Table 1 Directions of the electric and magnetic surface currents in the dual-band unit in Figures 8 and 9.

Frequency band	Sources	
	Electric current ($\vec{J}$)	Magnetic current ($\vec{M}$)
Polarization in lower band	$\hat{x}$, $\hat{v}$	$\hat{x}$, $\hat{y}$
Polarization in upper band	$\hat{y}$	$\hat{u}$, $\hat{v}$

With reference to Figure 10(b), over a wide range of frequency (except at the end of the band) radiation patterns of the antenna feature almost symmetric and side-lobe free patterns, which occur due to the uniform distributions of the electromagnetic (EM) field over the antenna's aperture. Due to the design flexibility in the antenna's structure, as suggested by the parametric analysis, the antenna offers tunable input impedance in terms of the reactance and resistance parts, which makes it suitable for direct integration with active components. Notably, the reactance part can be also tuned, to some extent, by altering the distance between the radiating unit and the ground plane (i.e., antenna profile). Depending on the frequency ratio between bands, this reactive contribution could be coherent (capacitive/capacitive or inductive/inductive) or incoherent (capacitive/inductive or inductive/capacitive) in the lower and upper frequency bands. It is worth mentioning that the variation of the inter-element gap (c.f. Figure 8) shows negligible effects on the upper frequency band. Therefore, we do not consider it for the sake of brevity.

V. Prototyping of the Dual-Band Radiating Surface

With reference to Figure 1, in which a 2 × 2 arrangement of the developed dual-band radiating surface is shown (c.f. Figures 8 and 10), a larger radiating surface is realized, which can operate in three frequency bands. However, in this section, a 2 × 1 array arrangement of the radiating unit (corresponding to 2 × 4 array of the ME-dipole-alike antenna) operating at the Ku-band and Ka-band is designed and fabricated as proof of concept.

The different views of the proposed five-layer antenna are provided in Figure 11. The radiating aperture is at the topmost layer, while all the feeding lines are designed at the bottom layer. Rogers RO3006 with a relative permittivity of 6.5 and thickness of 10 mils was employed at the bottom layer, while Rogers RT Duroid 5880 with a thickness of 31, 10, 31, and 10 mils (from the bottom to the top layer) was employed for the upper layers to reduce the surface wave effects and improve the radiation performances. All substrate layers were glued using epoxy. Then, they were heated and pressed to establish a uniform connection between the layers, according to the PCB fabrication process

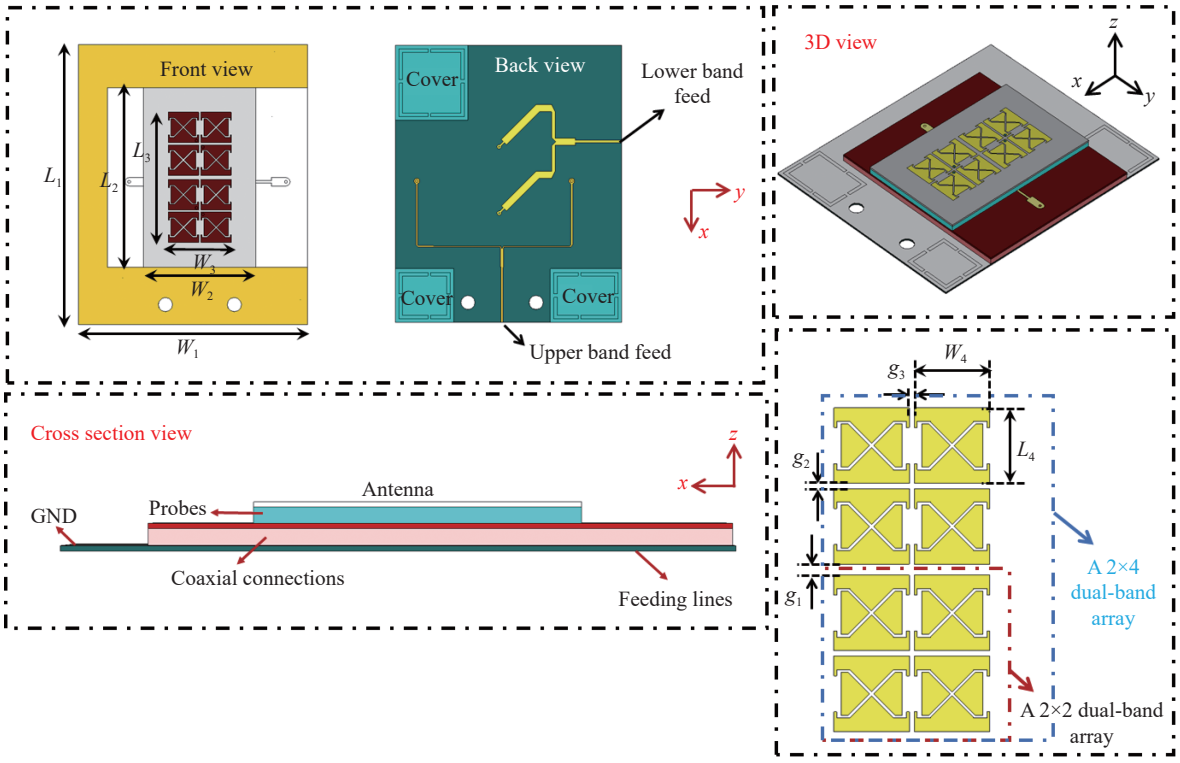

Figure 11 Different views of the developed prototype along with some main dimensions (L_1 = 38.8 mm, W_1 = 31.65 mm, L_2 = 24.8 mm, W_2 = 15.5 mm, L_3 = 18 mm, W_3 = 8.7 mm, g_1 = 0.6 mm, g_2 = 0.3 mm, g_3 = 0.3 mm, L_4 = 4.2 mm and W_4 = 4.2 mm.

available in our Poly-Grames Research Center. Conductive adhesive has been employed to make electrical connections between the two adjacent ground planes in the bottom layers.

It is worth emphasizing that all the feeding networks have been transferred to the bottommost layer, and a relatively high-permittivity substrate has been subsequently used for this layer, as this technique provides a solution for seamless integration of the antenna with frontend [6], [38]. Moreover, although the presented methodology can be adopted for a wide variety of high-κ substrates with much larger relative permittivity, due to some restrictions imposed by our PCB fabrication process, we used a substrate with $\varepsilon_r = 6.5$. To reduce the devastating and parasitic effects of the surface waves on the radiation patterns, particularly in the Ka-band, some free spaces on the surface of the dielectric were covered by a metallic cover and surrounded by SIW walls to prevent the propagation of the surface waves as well as the parallel plate modes.

1. Feeding network in Ka-band

As mentioned earlier, each ME-dipole antenna operates individually in the upper frequency band. As shown in Figure 12, all antennas were excited by the coupling of eight narrow strips to the antennas at their centers. Then, two four-way microstrip power dividers were designed and connected to the strips through eight metalized vias. Subsequently, two-way microstrip power dividers were designed at the bottom layer and connected to the top power dividers by two 15-mil diameter pins, which were soldered and then polished at both the top and bottom layers. To reduce the parasitic effects (including the reactive and radiation effects) of the pins, they were shielded by two large, metalized holes that operate as coaxial-like transmission lines (CLTL), as depicted in Figure 12(b). The parasitic radiation of the two pins at both sides [right and left sides in Figure 12(a)] of the antenna results in the formation of nulls and deviations of the radiation pattern. To circumvent this issue, a slight asymmetry was introduced on the right side of the two-way power divider at the bottommost layer [c.f. Figure 12(a)].

By introducing this asymmetry in the feeding network, the phase of the surface currents over the pins is altered, thus resulting in a controlled parasite radiation that provides more coherent effects on the main lobe. As a result, by optimizing the positions of the pins, the adverse effects of the parasitic radiation on the main radiation pattern are minimized. In this case, the asymmetry in the two-way power divider is also adjusted to achieve optimal results for both the radiation pattern and return loss.

2. Feeding network in Ku-band

In this Ku-frequency band, the radiating surface operates as a 2 × 1 arranged array along the x-axis, as shown in Figure 13 (a). Although the radiating surfaces can be excited by the coupling of two diagonally oriented [along the v-axis in Figure 8(a)] strips to the aperture, due to restrictions imposed by our PCB fabrications, two pairs of pins electrically connected to the radiating surfaces are used for excitations. The two pairs of pins connect the radiating surfaces

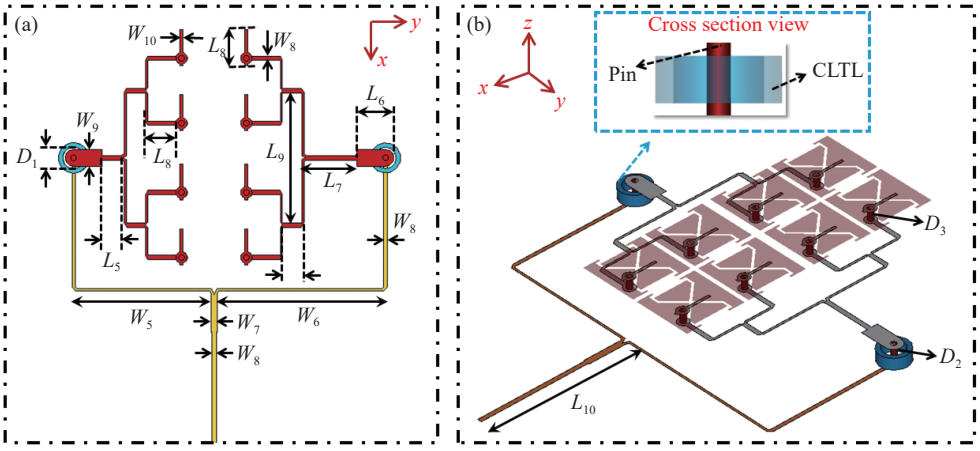

Figure 12 Details of the feeding network in the Ka-band ($W_5 = 9.45$ mm, $W_6 = 11.58$ mm, $W_7 = 0.46$ mm, $W_8 = 0.31$ mm, $W_9 = 1.16$ mm, $W_{10} = 0.2$ mm, $L_5 = 1.32$ mm, $L_6 = 2.5$ mm, $L_7 = 3.47$ mm, $L_8 = 2.5$ mm, $L_9 = 9$ mm, $L_{10} = 10.4$ mm, $D_1 = 1.5$ mm, $D_2 = 0.4$ mm and $D_3 = 0.4$ mm.

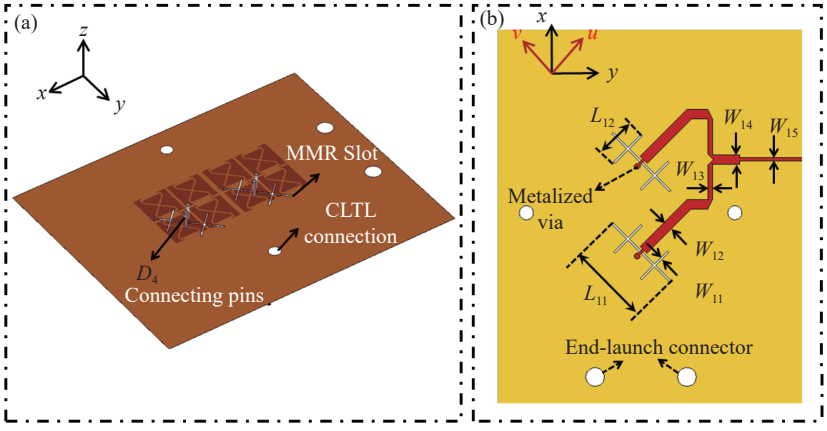

Figure 13 Details of the feeding network of the lower frequency band (Ku-band) ($W_{11} = 0.2$ mm, $W_{12} = 1$ mm, $W_{13} = 0.5$ mm, $W_{14} = 1$ mm, $W_{15} = 0.34$ mm, $L_{11} = 8.5$ mm and $L_{12} = 4$ mm.

to the narrow multimode resonance (MMR) slot [36] etched on the ground plane. The paired pins operate as differential transmission lines. Therefore, they present negligible parasitic effects on the antenna performance. The MMR slots [which are oriented along the v-axis in Figure 13(b)] are set to enhance the impedance matching between the feeding lines and the antenna while requiring less space as compared to simple slots.

The connecting pins were soldered and then completely polished at both ends to eliminate parasitic effects. A two-way microstrip power divider at the bottom layer feeds the two MMR slots. To enhance the EM coupling and eventually the impedance matching between the power divider and the radiating surface, the MMR concept and the step impedance technique were used [41]–[43]. Then, a high impedance microstrip line was electrically shorted to the ground plane through the two metallized vias. Reactive effects of the step impedance discontinuity along with the use of a high impedance microstrip line over the narrow MMR slot enhance the impedance matching conditions over a wide frequency range. In this scenario, a high impedance microstrip line increases the current intensity and the magnetic field around the slot. Since the coupling between the narrow MMR slots and microstrip lines are mostly governed by the magnetic field, the impedance matchings are improved.

VI. Simulations and Measurements

The fabricated prototype is shown in Figure 14. The reflection coefficient and realized gain were measured by the Keysight network analyzer (PNA N5247B) and at the far-field anechoic chamber of our Poly-Grames Research Cen-

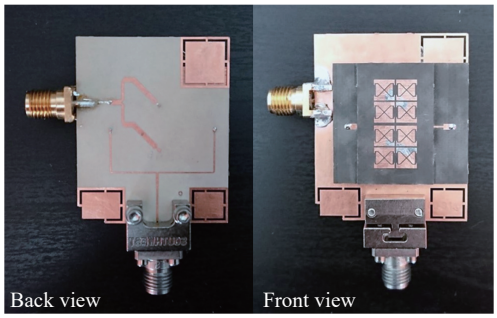

Figure 14 The top and bottom views of the fabricated prototype.

ter, respectively. The results are depicted in Figure 15. The simulated and measured peak gains in the Ku-band are around 7.3 and 7dBi, respectively, and the values for the impedance bandwidth are 41.2% (12.5 to 19 GHz) and 30% (12 to 16.2 GHz). An approximately 10% reduction in the bandwidth is observed. This reduction may be attributed to the fabrication tolerances. The simulated and measured 3-dB gain bandwidths are 37.8% (12 GHz to 17.6 GHz) and 25.4% (12 to 15.5 GHz), respectively. In the Ka-band, the simulated and measured peak gains are 8.9 dBi and 8 dBi, respectively, while the simulated and measured impedance bandwidths are 13.14% (32 GHz to 36.5 GHz) and 10.65% (32 GHz to 35.6 GHz), respectively. The simulated and measured 3-dB gain bandwidths are 12.6% (32 to 36.3 GHz) and 8.52% (32 to 34.85 GHz), respectively.

Some discrepancies and minor frequency shifts observed in the measured reflection coefficient can be attributed to the tolerances within our complex multilayer fabrication process. The maximum simulated (and measured) in-band mutual couplings in the lower and upper frequency bands are approximately −14 dB (−16.65 dB) and −27.8 dB (−32.3 dB), respectively. The maximum simulated radiation efficiencies for both the lower and upper frequency bands are approximately 80%.

Due to the efficient reuse of the antenna's aperture in both frequency bands, the aperture-reused efficiency is 100% in the proposed dual-band aperture-shared radiating surface. The simulated and measured radiation patterns of the antenna in the Ku-band are plotted for two frequencies of 13 and 15 GHz in Figure 16, which shows a well-pronounced agreement between the simulation and measurement results. The radiation patterns of the proposed prototype in the Ka-band are measured and compared with the simulation

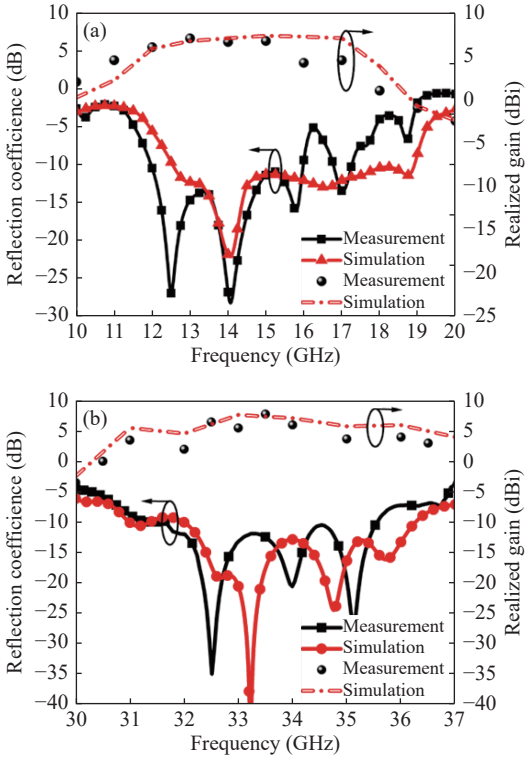

Figure 15 Measured and simulated reflection coefficiencts and realized gains of the antenna in the (a) Ku-band and (b) Ka-band.

results in Figure 17 at 33 and 36 GHz. Moreover, the simulation and measurement results have good agreements. Notably, due to the parasitic effects of the connecting pins, some deviations are observed in the radiation patterns particularly in the E-plane. To highlight the performance of the proposed dual-band antenna array, a comparative table (Table 2) is provided. The proposed radiating surface out-

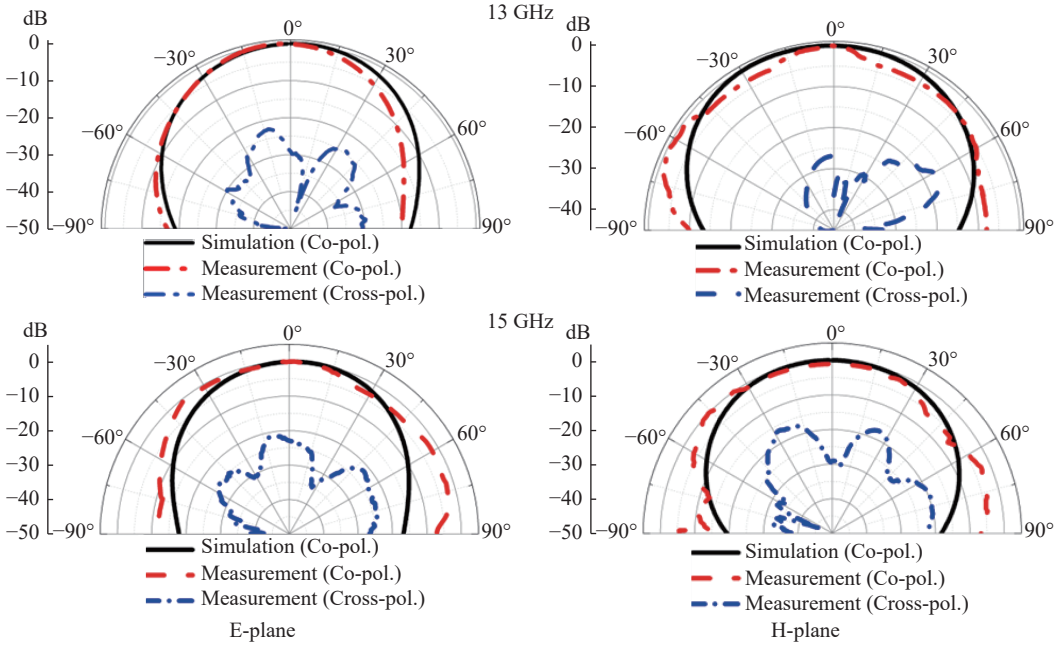

Figure 16 E-plane and H-plane cuts of the radiation patterns for two frequencies (13 and 15 GHz) in the Ku-band.

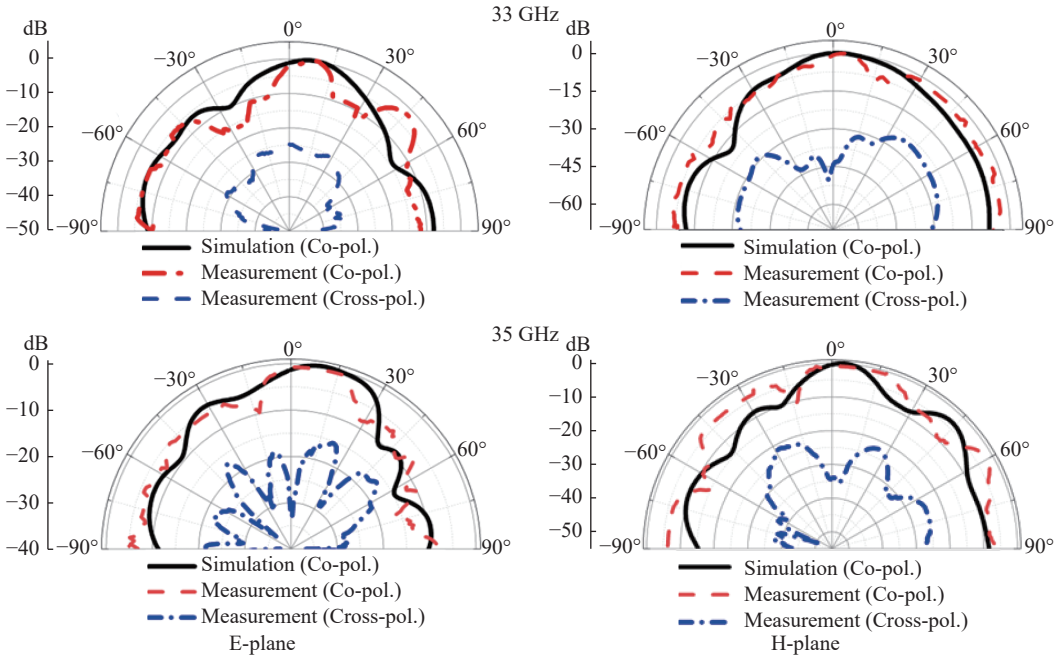

Figure 17 E-plane and H-plane cuts of radiation patterns for two frequencies (33 and 35 GHz) in the Ka-band.

Table 2 Comparison of the proposed and reference antenna arrays

Ref	Frequency bands	Imped. BW (%)	Gain BW (%)	No. of freq. bands	Aperture-reused ratio	Seamless integration	Fabrication process
[6]	S/Ka	3.12/9.6	3/3	Two (Fixed)	1	Yes	2-layer standard PCB
[8]	S/Ka	11.7/11.9	15/13.5	Two (Fixed)	–	No	4-layer standard PCB
[9]	S/Ka	7.4/12.1	7/14	Two (Fixed)	–	No	5-layer standard PCB
[10]	S/V	5.3/6.4	–	Two (Fixed)	0.77	No	3-layer standard PCB
[20]	S/Ka	3.2/2	–	Two (Fixed)	1	No	2-layer standard PCB
This work (simulated)	**Ku-band**	**41.2**	**37.8**	**Two (Extendable to multiband)**	**1**	**Yes**	5-layer standard PCB
	Ka-band	**13.14**	**12.6**				
This work (measured)	**Ku-band**	**30**	**25.4**				
	Ka-band	**10.65**	**8.52**				

performs other published works, as determined from the combination of the aperture-reused ratio, impedance and gain bandwidth, seamless integration with active circuits, and ability to operate in multiple frequency bands. Due to the complex structure of the proposed antenna array, the antenna array performance would be closely dependent on the quality of the fabrication process.

VII. Conclusion

In this work, we proposed and investigated a concept based on convolving magnetic and electric surface currents for the development of multi-band radiating surfaces. We demonstrated that a dual-band radiating surface can be realized by a 2 × 2 arrangement of the developed single band antenna. Subsequently, a tri-band radiations can be realized by a 4 × 4 arrangement of the single band antenna. As a proof of concept, an array of a 1 × 2 dual-band antenna was designed and fabricated using a cost-effective multi-layer PCB process. In this prototype, we transferred all feeding lines to the bottom-most layer with a relative permittivity of $\epsilon_r = 6.5$, while the top layers were implemented on substrates with low permittivity. In this scenario, the antenna benefits from both the high radiation performance and the seamless integration with active circuits. The dual-band antenna was fabricated and demonstrated, and a comparison of the measurement and simulation results shows good agreements.

Acknowledgements

The authors would like to thank all the technical staff in the Poly-Grames Research Center, particularly Mr. Traian Antonescu, for their assistance in the fabrications and measurements. We would also like to acknowledge the support of the National Research Council Canada's high throughput and secure networks (HTSN) research program.

References

[1] L. Chioukh, H. Boutayeb, L. Li, *et al*., "Integrated radar systems for precision monitoring of heartbeat and respiratory status," in *Asia*

Pacific Microwave Conference, Singapore, pp. 405–408, 2009.

[2] P. Burasa, N. G. Constantin and K. Wu, "High-efficiency wideband rectifier for single-chip batteryless active millimeter-wave identification (MMID) Tag in 65-nm Bulk CMOS technology," *IEEE Transactions on Microwave Theory and Techniques*, vol. 62, no. 4, pp. 1005–1011, 2014,

[3] J. Moghaddasi and K. Wu, "Multifunctional transceiver for future radar sensing and radio communicating data-fusion platform," *IEEE Access*, vol. 4, pp. 818–838, 2016,

[4] P. Burasa, T. Djerafi, N. G. Constantin, *et al*., "High-data-rate single-chip battery-free active millimeter-wave identification tag in 65-nm CMOS technology," *IEEE Transactions on Microwave Theory and Techniques*, vol. 64, no. 7, pp. 2294–2303, 2016,

[5] P. Burasa, T. Djerafi, N. G. Constantin, *et al*., "On-chip dual-band rectangular slot antenna for single-chip millimeter-wave identification tag in standard CMOS technology," *IEEE Transactions on Antennas and Propagation*, vol. 65, no. 8, pp. 3858–3868, 2017,

[6] A. Askarian, J. P. Yao, Z. G. Lu, *et al*., "Leaky-wave radiating surface on heterogeneous high-κ material for monolithic antenna-frontend integration," *Journal of Applied Physics*, vol. 133, no. 7, article no. 074502, 2023,

[7] A. Askarian and K. Wu, "Shared-aperture enabled integration of Sub-6 GHz and millimeter-wave antennas for future multi-functional wireless systems," in *2020 IEEE International Symposium on Antennas and Propagation and North American Radio Science Meeting*, Montreal, QC, Canada, pp. 1775–1776, 2020.

[8] X. H. Ding, W. W. Yang, W. Qin, *et al*., "A broadside shared aperture antenna for (3.5, 26) GHz mobile terminals with steerable beam in millimeter-waveband," *IEEE Transactions on Antennas and Propagation*, vol. 70, no. 3, pp. 1806–1815, 2022,

[9] X. H. Ding, W. W. Yang, H. Tang, *et al*., "A dual-band shared-aperture antenna for microwave and millimeter-wave applications in 5G wireless communication," *IEEE Transactions on Antennas and Propagation*, vol. 70, no. 12, pp. 12299–12304, 2022,

[10] J. F. Zhang, Y. J. Cheng, Y. R. Ding, *et al*., "A dual-band shared-aperture antenna with large frequency ratio, high aperture reuse efficiency, and high channel isolation," *IEEE Transactions on Antennas and Propagation*, vol. 67, no. 2, pp. 853–860, 2019,

[11] G. H. Xu, L. X. Yang, Z. X. Huang, *et al*., "Microstrip grid and patch-based dual-band shared-aperture differentially fed array antenna," *IEEE Antennas and Wireless Propagation Letters*, vol. 20, no. 6, pp. 1043–1047, 2021,

[12] Z. J. Guo, Z. C. Hao, H. Y. Yin, *et al*., "Planar shared-aperture array antenna with a high isolation for millimeter-wave low earth orbit satellite communication system," *IEEE Transactions on Antennas and Propagation*, vol. 69, no. 11, pp. 7582–7592, 2021,

[13] J. Lan, Z. Q. Yu, J. Y. Zhou, *et al*., "An aperture-sharing array for (3.5, 28) GHz terminals with steerable beam in millimeter-wave band," *IEEE Transactions on Antennas and Propagation*, vol. 68, no. 5, pp. 4114–4119, 2020,

[14] Y. Qin, R. L. Li, Q. Xue, *et al*., "Aperture-shared dual-band antennas with partially reflecting surfaces for base-station applications," *IEEE Transactions on Antennas and Propagation*, vol. 70, no. 5, pp. 3195–3207, 2022,

[15] J. F. Zhu, Y. Yang, S. W. Liao, *et al*., "Aperture-shared millimeter-wave/Sub-6 GHz dual-band antenna hybridizing Fabry–Pérot cavity and Fresnel zone plate," *IEEE Transactions on Antennas and Propagation*, vol. 69, no. 12, pp. 8170–8181, 2021,

[16] P. Mei, S. Zhang and G. F. Pedersen, "A dual-polarized and high-Gain X-/Ka-band shared-aperture antenna with high aperture reuse efficiency," *IEEE Transactions on Antennas and Propagation*, vol. 69, no. 3, pp. 1334–1344, 2021,

[17] C. L. Chen, "A dual wideband compact shared-aperture Microstrip patch/Fabry–Perot resonator cavity antenna," *IEEE Transactions on Antennas and Propagation*, vol. 70, no. 12, pp. 11526–11536, 2022,

[18] Z. G. Liu, R. J. Yin and W. B. Lu, "A novel dual-band shared-aperture antenna based on folded reflectarray and Fabry–Perot cavity," *IEEE Transactions on Antennas and Propagation*, vol. 70, no. 11, pp. 11177–11182, 2022,

[19] Z. G. Liu, R. J. Yin, Z. N. Ying, *et al*., "Dual-band and shared-aperture Fabry–Perot cavity Antenna," *IEEE Antennas and Wireless Propagation Letters*, vol. 20, no. 9, pp. 1686–1690, 2021.

[20] J. F. Zhu, Y. Yang, S. W. Liao, *et al*., "Dual-band aperture-shared Fabry–perot cavity-integrated patch antenna for millimeter-wave/Sub-6 GHz communication applications," *IEEE Antennas and Wireless Propagation Letters*, vol. 21, no. 5, pp. 868–872, 2022,

[21] C. X. Bai, Y. J. Cheng, Y. R. Ding, *et al*., "A metamaterial-based *S/X*-band shared-aperture phased-array antenna with wide beam scanning coverage," *IEEE Transactions on Antennas and Propagation*, vol. 68, no. 6, pp. 4283–4292, 2020,

[22] C. F. Zhou, S. S. Yuan, H. Li, *et al*., "Dual-band shared-aperture antenna with bifunctional metasurface," *IEEE Antennas and Wireless Propagation Letters*, vol. 20, no. 10, pp. 2013–2017, 2021,

[23] T. Li and Z. N. Chen, "Metasurface-based shared-aperture 5G *S-/K*-band antenna using characteristic mode analysis," *IEEE Transactions on Antennas and Propagation*, vol. 66, no. 12, pp. 6742–6750, 2018,

[24] A. Askarian and K. Wu, "Miniaturized dual-band slot antenna with self-scalable pattern for array applications," in *2020 IEEE International Symposium on Antennas and Propagation and North American Radio Science Meeting*, Montreal, QC, Canada, pp. 1943–1944, 2020.

[25] Y. R. Ding and Y. J. Cheng, "Ku/Ka dual-band dual-polarized shared-aperture beam-scanning antenna array with high isolation," *IEEE Transactions on Antennas and Propagation*, vol. 67, no. 4, pp. 2413–2422, 2019,

[26] K. Li, T. Dong and Z. H. Xia, "A broadband shared-aperture L/S/X-band dual-polarized antenna for SAR applications," *IEEE Access*, vol. 7, pp. 51417–51425, 2019,

[27] C. X. Mao, S. Gao, Q. Luo, *et al*., "Low-Cost X/Ku/Ka-band dual-polarized array with shared aperture," *IEEE Transactions on Antennas and Propagation.*, vol. 65, no. 7, pp. 3520–3527, 2017,

[28] P. Mei, X. Q. Lin, G. F. Pedersen, *et al*., "Design of a triple-band shared-aperture antenna with high figures of merit," *IEEE Transactions on Antennas and Propagation*, vol. 69, no. 12, pp. 8884–8889, 2021,

[29] M. T. Wang and C. H. Chan, "A Novel differentially-fed dual-polarized shared aperture antenna Array," *IEEE Transactions on Antennas and Propagation.*, vol. 70, no. 12, pp. 12276–12281, 2022,

[30] S. Trinh-Van, T. Van Trinh, Y. Yang, *et al*., "Bandwidth-enhanced low-profile magneto-electric dipole antenna with shorting parasitic elements," *IEEE Access*, vol. 9, pp. 64852–64859, 2021,

[31] J. W. Li, Y. Hu, L. Xiang, *et al*., "Broadband circularly polarized magnetoelectric dipole antenna and array for K-band and Ka-band satellite communications," *IEEE Transactions on Antennas and Propagation*, vol. 70, no. 7, pp. 5907–5912, 2022,

[32] M. T. Wang and C. H. Chan, "Dual-polarized, low-profile dipole-patch array for wide bandwidth applications," *IEEE Transactions on Antennas and Propagation*, vol. 70, no. 9, pp. 8030–8039, 2022,

[33] J. Xu, W. Hong, Z. H. Jiang, *et al*., "Low-cost millimeter-wave circularly polarized planar integrated magneto-electric dipole and its arrays with low-profile feeding structures," *IEEE Antennas and Wireless Propagation Letters*, vol. 19, no. 8, pp. 1400–1404, 2020,

[34] S. J. Yang, Y. M. Pan, Y. Zhang, *et al*., "Low-profile dual-polarized filtering magneto-electric dipole antenna for 5G applications," *IEEE Transactions on Antennas and Propagation*, vol. 67, no. 10, pp. 6235–6243, 2019,

[35] L. Siu, H. Wong and K. M. Luk, "A dual-polarized magneto-electric dipole with dielectric loading," *IEEE Transactions on Antennas and Propagation*, vol. 57, no. 3, pp. 616–623, 2009,

[36] W. J. Lu and L. Zhu, "Wideband stub-loaded slotline antennas under multi-mode resonance operation," *IEEE Transactions on Antennas and Propagation*, vol. 63, no. 2, pp. 818–823, 2015,
[37] A. Askarian, J. Yao, Z. Lu, *et al*., "Surface-wave control technique for mutual coupling mitigation in array antenna," *IEEE Microwave and Wireless Components Letters*, vol. 32, no. 6, pp. 623–626, 2022,
[38] A. Askarian, J. P. Yao, Z. G. Lu, *et al*., "Extremely low-profile periodic 2-D leaky-wave antenna: An optimal solution for antenna-frontend integration," *IEEE Transactions on Antennas and Propagation*, vol. 70, no. 9, pp. 7798–7812, 2022,
[39] S. N. Nallandhigal and K. Wu, "Unified and integrated circuit antenna in front end—A proof of concept," *IEEE Transactions on Microwave Theory and Techniques*, vol. 67, no. 1, pp. 347–364, 2019,
[40] W. Liu, Z. N. Chen and X. Qing, "Metamaterial-based low-profile broadband aperture-coupled grid-slotted patch antenna," *IEEE Trans. actions on Antennas and Propagation*, vol. 63, no. 7, pp. 3325–3329, 2015,
[41] W. Menzel, L. Zhu, K. Wu, *et al*., "On the design of novel compact broad-band planar filters," *IEEE Transactions on Microwave Theory and Techniques*, vol. 51, no. 2, pp. 364–370, 2003,
[42] L. Zhu, S. Sun and W. Menzel, "Ultra-wideband (UWB) bandpass filters using multiple-mode resonator," *IEEE Microwave and Wireless Components Letters*, vol. 15, no. 11, pp. 796–798, 2005,
[43] A. Askarian and K. Wu, "Wideband and high-gain slot antenna using self-scalable current distribution and multi-mode resonance," in *2021 IEEE 19th International Symposium on Antenna Technology and Applied Electromagnetics (ANTEM)*, Winnipeg, MB, Canada, pp. 1–2, 2021.

Amirhossein Askarian received the M.S. degree (Hons.) in electrical engineering from Amirkabir University of Technology (AUT), Tehran, Iran in 2013, and the Ph.D. degree in electrical engineering from Polytechnique Montreal (University of Montreal), Canada, in 2023. In 2018, he joined the Poly-Grames Research Center, École Polytechnique de Montréal, as a Research Assistant. Currently he is working as a Senior RF Design Engineer at Ciena, where he is responsible for maintaining signal integrity in RFIC packaging. His current research interests include high speed I/O interconnects, signal and power integrity, ultrawideband transmission line, planar (2D) leaky-wave antennas, active integrated antenna arrays (AiA), antenna-on-chip (AoC) and microwave and RF circuits design. Dr. Askarian was a recipient of the Honorable Mention Award in IEEE AP-S 2020 Conference in Montreal, Canada.
(Email: a.askarian@polymtl.ca)

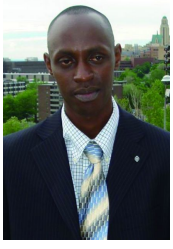

Pascal Burasa received the B.S., M.S., and Ph.D. degrees (Hons.) in electrical engineering from the École Polytechnique de Montréal (University of Montreal), Montreal, QC, Canada, in 2006, 2008, and 2016, respectively. From 2008 to 2010, he was with the Microelectronic Research Group, École Polytechnique de Montréal, where he developed CMOS color image sensors free of optic filters. He is currently a Researcher with the Poly-Grames Research Center, École Polytechnique de Montréal. He has authored or coauthored several peer-reviewed journal articles and conference papers. He holds several patents. His research interests include microelectronic circuits and systems operating at millimeter-wave and terahertz (THz) frequencies for radar, imaging, wireless sensing, and ultrahigh-speed communication applications, including millimeter-wave/terahertz reconfigurable transceiver architectures and components for multifunction wireless systems.
(Email: pascal.burasa@polymtl.ca)

Ke Wu received the B.S. degree (Hons.) in radio engineering from Nanjing Institute of Technology (now Southeast University), Nanjing, China, in 1982, the D.E.A. degree (Hons.) and the Ph.D. degree (Hons.) in optics, optoelectronics, and microwave engineering, respectively in 1984 and 1987, all from the Institut National Polytechnique de Grenoble (INPG) and the University of Grenoble, Grenoble, France.

He was the Founding Director of the Center for Radio Frequency Electronics Research of Quebec (Regroupement stratégique of FRQNT) and the Canada Research Chair of RF and Millimeter-wave Engineering. He is currently a Professor of electrical engineering and the Industrial Research Chair in Future Wireless Technologies with the Polytechnique Montréal (University of Montreal), where he is the Director of the Poly-Grames Research Center. He has authored or coauthored over 1400 referred articles and numerous books/book chapters and filed over 80 patents. His current research interests involve substrate integration technologies, antenna arrays, field theory and joint field/circuit modeling, ultrafast guided-wave electronics, wireless power transfer and harvesting, microwave photonics, and MHz-through-THz technologies and transceivers including RFICs/MMICs for joint radar/communication architectures, innovative multifunction wireless systems, and biomedical applications.

Dr. Wu is a Fellow of the IEEE, the Canadian Academy of Engineering, the Academy of Science of the Royal Society of Canada, and the German National Academy of Science and Engineering (acatech). He is a member of the Electromagnetics Academy, URSI, and IEEE-Eta Kappa Nu (IEEE-HKN). He was a recipient of many awards and prizes including the inaugural IEEE MTT-S Outstanding Young Engineer Award, the 2004 Fessenden Medal of the IEEE Canada, the 2009 Thomas W. Eadie Medal of the Royal Society of Canada, the Queen Elizabeth II Diamond Jubilee Medal in 2013, the 2013 FCCP Education Foundation Award of Merit, the 2014 IEEE MTT-S Microwave Application Award, the 2014 Marie-Victorin Prize (Prix du Quebec), the 2015 Prix d'Excellence en Recherche et Innovation of Polytechnique Montréal, the 2015 IEEE Montreal Section Gold Medal of Achievement, the 2019 IEEE MTT-S Microwave Prize, the 2021 EIC Julian C. Smith Medal, the 2022 IEEE MTT-S Outstanding Educator Award, and the 2022 IEEE AP-S John Kraus Antenna Award. He has held key positions in and has served on various panels and international committees including the Chair of technical program committees, international steering committees, and international conferences/symposia. In particular, he was the General Chair of the 2012 IEEE Microwave Theory and Techniques (IEEE MTT-S) International Microwave Symposium (IMS) and TPC Co-Chair of the 2020 IEEE International Symposium on Antennas and Propagation (APS). He has served on the editorial/review boards for many technical journals, transactions, proceedings, and letters as well as scientific encyclopedia including editor, track editor, and guest editor. He was the Chair of the joint IEEE Montreal chapters of MTT-S/AP-S/LEOS and then the restructured IEEE MTT-S Montreal Chapter, Canada. He has served the IEEE MTT-S Administrative Committee (AdCom) as the Chair for the IEEE MTT-S Transnational Committee, the Member and Geographic Activities (MGA) Committee, Technical Coordinating Committee (TCC), and the 2016 IEEE MTT-S President among many other AdCom functions. He is currently the Chair of the IEEE MTT-S Inter-Society Committee. He was a Distinguished Microwave Lecturer of the IEEE MTT-S from 2009 to 2011. He served the European Microwave Association (EuMA) as the Inaugural Representative of North America in its General Assembly.
(Email: ke.wu@polymtl.ca)